ACS Energy LETTERS

http://pubs.acs.org/journal/aelccp

LETTER

Quadruple-Cation Wide-Bandgap Mixed-Halide Tin Perovskite Solar Cells

Chun-Hsiao Kuan, Yu-Cheng Chen, Sudhakar Narra, Chun-Fu Chang, Yi-Wei Tsai, Jhih-Min Lin, Guan-Ruei Chen, and Eric Wei-Guang Diau*

Cite This: *ACS Energy Lett.* 2024, 9, 2351−2357

Read Online

ACCESS | Metrics & More | Article Recommendations | Supporting Information

ABSTRACT: Tin-based perovskite solar cells (TPSCs) are a promising alternative to the traditional lead-based PSCs for lead-free photovoltaic applications. To further promote the performance and stability, a tandem type of TPSC is an attractive direction to pursue. To serve as a low-bandgap TPSC with the bandgap (E_g) of around 1.4 eV, searching for a high-bandgap TPSC with an E_g in the range 1.8−2.0 eV is an important task to build a lead-free tandem TPSC. Herein, we report the first quadruple-cation wide-bandgap TPSC with the perovskite structure of $FA_{0.55}MA_{0.25}Cs_{0.1}PMA_{0.1}SnBr_2I$ (FA, formamidinium; MA, methylammonium; PMA, phenylmethylammonium) and an E_g of 1.93 eV to give the efficiency of power conversion of 6.2%. We found that PMA plays a key role in passivating the grain surface of perovskites and the interface between the perovskite and the hole-transport layer to give high performance and great stability for a wide-bandgap TPSC with a quadruple-cation configuration.

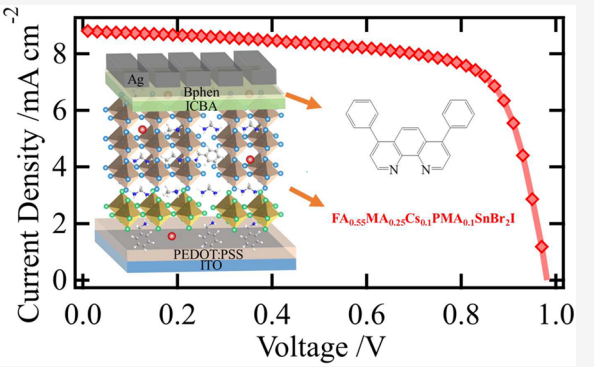

Perovskite solar cells (PSCs) are attractive next-generation solar cells because their best power conversion efficiency (PCE) has already reached 26.1%.[1] To further enhance the device performance for PSCs, development of all-perovskite tandem solar cells becomes a promising approach for scientists to pursue.[2−4] With the efforts on adjusting bandgaps (E_g) of perovskites, such as the wide-bandgap lead-based perovskite with an E_g of ∼1.6 eV and the narrow-bandgap tin−lead PSC with an E_g of ∼1.2 eV, the performance of the lead-based tandem PSCs can now reach the efficiency of power conversion (PCE) of 28%.[5,6] Additionally, the wide-bandgap lead-based perovskite can be effectively combined with narrow-bandgap materials such as monocrystalline silicon to form perovskite−silicon tandem solar cells to attain a remarkable PCE as high as 33.9%.[1] However, the above-mentioned tandem PSCs contain the toxic lead element that needs to be replaced by other nontoxic alternatives like tin.[7−10] Therefore, tin-based PSCs (TPSCs) have emerged rapidly, offering a viable replacement for their traditional lead-based counterparts.[11−17] The efficiency of a narrow-bandgap single-junction TPSC has increased to 14.8%,[18] and the development of lead-free tandem PSCs is one direction to go.[8−10] Differing from traditional lead-based tandem PSCs, achieving high performance for a fully lead-free tandem PSC is a challenging task.[19] In such a tandem architecture, because the high-performance narrow-bandgap perovskite has an E_g of ∼1.4 eV, a suitable wide-bandgap perovskite should have an E_g of 1.8−2.0 eV. To search for such a lead-free wide-bandgap perovskite, increasing the bromine ratio at the X-site is a promising approach.[20] Hao et al.[21] were the first ones to investigate a high-bandgap TPSC with varied X-site halides for the perovskite $MASnX_3$ (MA represents methylammonium) in a normal (n-i-p) device configuration, but they encountered significant voltage loss to give a limited PCE. Nevertheless, the $MASnBr_2I$ perovskite has an E_g of 1.75 eV that is close to what we need for a wide-bandgap perovskite in a tin-based tandem cell. In 2023, Martani et al.[22] introduced an FA/Cs (FA represents formamidinium) wide-bandgap TPSC, but the small size of Cs^+ caused a spectral redshift, limiting the E_g to around 1.7 eV in an equal bromine−iodine system with a PCE of 0.59%. Further research indicates that a bromine to iodine ratio greater than 1.5:1.5 in perovskite often leads to phase segregation, hindering performance enhancement under Br-rich conditions.[20,22] Therefore, the present study aims to search for a suitable wide-bandgap TPSC with a

Received: March 19, 2024
Revised: April 11, 2024
Accepted: April 19, 2024
Published: April 23, 2024

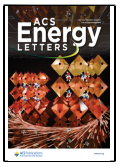

Br-rich X-site (Br_2I) and modification of the A-site cations to stabilize the perovskite phase at the same time to increase the E_g into the favorable range of 1.8−2.0 eV.

Herein, we introduce a quadruple-cation perovskite system to solve the problem of phase segregation for the Br_2I tin perovskite that contains 55% FA^+, 25% MA^+, 10% Cs^+, and 10% PMA^+ ($FA_{0.55}MA_{0.25}Cs_{0.1}PMA_{0.1}SnBr_2I$, abbreviated as PMA) with a favorable E_g of 1.93 eV for a high-bandgap TPSC (PMA, phenylmethylammonium; Figure 1). The selection of

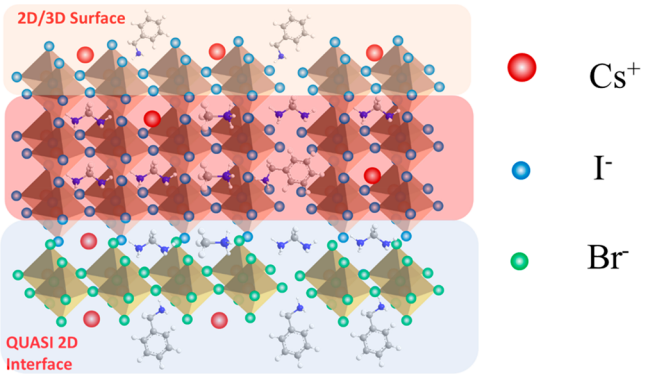

Figure 1. Schematic demonstration of the chemical structure for quadruple-cation wide-bandgap tin perovskite material $FA_{0.55}MA_{0.25}Cs_{0.1}PMA_{0.1}SnBr_2I$ (abbreviated as PMA).

these A-site cations was based on their device performance optimization procedure starting from the basic perovskite $FASnBr_2I$. As shown in Figure S1, $FA_{0.75}MA_{0.25}SnBr_2I$ (abbreviated as FAMA), $FA_{0.65}MA_{0.25}Cs_{0.1}SnBr_2I$ (abbreviated as Cs), and PMA were found to have the best performances by varying the ratios of the cations step by step. The incorporation of MA in $FASnBr_2I$ has the effect to improve both the V_{OC} and J_{SC}, but both values were still too low. Introducing a suitable amount of Cs^+ in FAMA perovskite helps to stabilize the phase and thus significantly enhances J_{SC}. To make a 2D/3D structure, eight bulky cations (Figure S2) were considered, from which PMA^+ stands out to significantly enhance the V_{OC} of the device (Figure S3). We found that PMA^+ not only binds with iodine vacancies on the surface for passivation but also forms a quasi-2D structure within the bulk. Interestingly, we found that PMA^+ also accumulates extensively at the bottom of the perovskite layer, creating a buried interface that passivates the segregated Br layer and forms a hole transport layer between perovskite and poly(3,4-ethylenedioxythiophene):poly(styrenesulfonate) (PEDOT:PSS), facilitating hole transport. To further improve the V_{OC}, indene-C60 bisadduct (ICBA) was used to replace C60.[16,17] However, the ICBA−bathocuproine (BCP) combination still poses challenges for effective electron transfer. Replacing BCP with bathophenanthroline (Bphen) markedly enhances the electron extraction efficiency. Ultimately, we succeeded in creating a hysteresis-free, quadruple-cation, wide-bandgap TPSC with an efficiency of 6.2%.

The X-ray photoelectron spectra (XPS) analyses of the FAMA, Cs, and PMA samples, as illustrated in Figures 2a−2c, revealed two key components: Sn^{2+} and Sn^{4+}. The XPS data suggest that the inclusion of Cs^+ and PMA^+ in the samples enhances the stability of the tin perovskite by reducing the

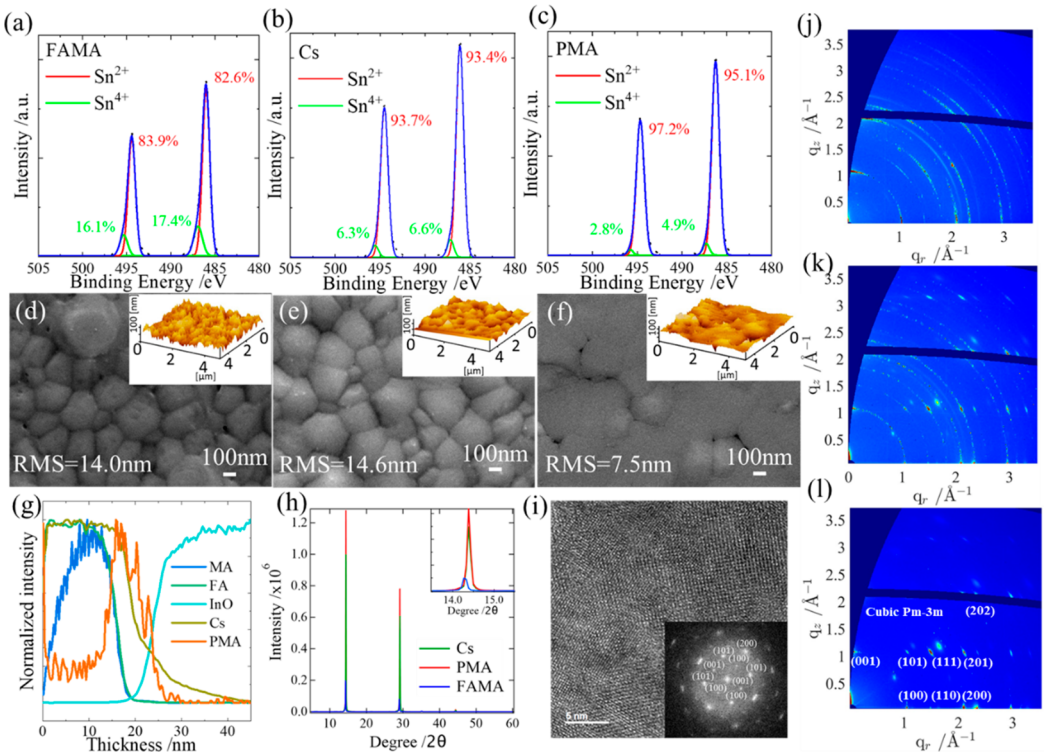

Figure 2. Characterizations of thin-film samples for the XPS spectra of (a) FAMA, (b) Cs, and (c) PMA showing the Sn^{2+}/Sn^{4+} proportions; the SEM and AFM images of (d) FAMA, (e) Cs, and (f) PMA showing the morphological characters; (g) TOF-SIMS distribution plots of the PMA sample; (h) XRD patterns of the Br_2I samples with varied A-site cations; (i) high-resolution transmission electron microscopy (HRTEM) of the PMA sample; and GIWAXS patterns of (j) FAMA, (k) Cs, and (l) PMA showing the preferred-orientation features of the crystals.

https://doi.org/10.1021/acsenergylett.4c00796
ACS Energy Lett. 2024, 9, 2351−2357

oxidation of Sn^{2+} on the surface. In particular, the PMA sample demonstrated the highest Sn^{2+}/Sn^{4+} ratio among the others, implying its superior performance and stability compared to those of the other samples. The SEM images reveal that the FAMA samples (Figure 2d) have larger grains, but their grain boundaries are indistinct, and there are noticeable holes and cracks on the surface. However, with the addition of Cs^+ (Figure 2e), the grains exhibit distinct boundaries and improved morphology, suggesting enhanced crystallinity in the Cs film. Furthermore, the introduction of PMA^+ (Figure 2f) results in a flattened surface, with the three-dimensional perovskite feature becoming less visible, indicative of the formation of a typical quasi-2D phase on the surface. This suggests that the PMA sample has a 2D/3D structure in the perovskite film. Atomic force microscopy (AFM) images shown in the insets of Figures 2d−2f reflect the surface roughness of the perovskite films. The surfaces treated with FAMA and Cs exhibited comparable levels of roughness, giving roughness RMS values of 14.0 and 14.6 nm, respectively. However, upon further incorporation of PMA, the surface morphology significantly improved, becoming flatter and smoother, with the roughness of RMS reducing to 7.5 nm.

Time-of-flight secondary-ion mass spectroscopy (TOF-SIMS) analysis reveals a particularly intriguing structural composition aspect for the PMA sample. In principle, the bulky organic cation PMA^+ should not insert into the A-site of the 3D perovskite structure but instead form the 2D phase on the surface. In contrast, our findings show that PMA^+ is thoroughly involved in the A-site position, which FA^+ and MA^+ cations occupy in the middle of the 3D perovskite film while Cs^+ appears to occupy in the whole place of the film. As shown in Figure 2g, PMA^+ exhibits a strong signal on the surface of the perovskite, suggesting its significant role in modifying the surface of the film to form the 2D structure (Figure 2f). Looking deeper into the perovskite film, PMA^+ does not occupy the middle of the film but a strong signal of PMA^+ can be found in bottom of the film, indicating the strong effect of penetration of the PMA^+ cation into the bottom interface of the film to form the 2D structure in the bottom of the perovskite film, as schematically demonstrated in Figure 1. The TOF-SIMS results lead us to infer that under certain conditions PMA^+ can insert deeply into the A-site position to form a 2D phase in the bottom of the perovskite structure. The engagement of the PMA^+ cation is believed to potentially reduce the movement of unstable bromine ions, thereby improving the stability of the perovskite film. Furthermore, effects such as passivation and modification are thought to modify the interface between the perovskite and the hole conductive layers. Consequently, our findings suggest that the involvement of PMA^+ could enhance the efficiency and stability of a TPSC, although further research is required for conclusive evidence.

X-ray diffraction (XRD) analysis revealed that the incorporation of Cs^+ and PMA^+ significantly enhances the cubic phase orientation in the perovskite film. The XRD patterns of the FAMA, Cs, PMA, and other quadruple-cation mixed-halide perovskites were analyzed using the total pattern solution (TOPAS) software. This analysis was conducted to determine the lattice parameters of the perovskite crystals, with the results presented in Figures S4−S9. The calculated lattice parameters derived from these simulations are summarized in Table S1. Incorporating Cs^+ and PMA^+ into the perovskite films results in a more pronounced perovskite diffraction peak, as evidenced by the greatly enhanced XRD intensities (Figure 2h). This suggests that both cations play a significant role in the crystal structure arrangement and enhance the overall crystallinity, thereby contributing to stabilization of the PMA (or Br_2I) structure. Additionally, a minor shift in angle was noted on the x-axis. For a clear comparison, the location of the main peak was magnified and superimposed, as depicted in the inset of Figure 2h. The XRD and TOPAS results are consistent with the sizes of all of the perovskites, according to the lattice parameters shown in Table S1. In summary, for the Br_2I perovskites, incorporation of the Cs^+ cation reduces the size of the unit cell in comparison with the FAMA sample. However, further incorporation of the PMA^+ only increases the size of the unit cell to a small extent, indicating that the PMA^+ cation is not involved in the 3D bulk phase of the perovskite structure. This is consistent with the TOF-SIMS results that the PMA^+ cation only involves the perovskite surface and the bottom interface between the perovskite and HTM layers. A high-resolution transmission electron microscopy (HRTEM) image of the PMA sample in a 5 nm scale is shown in Figure 2i with clear Bragg diffraction spots consistent with the XRD and TOPAS results.

We further delved into the crystallographic alignment of the preferred orientation of the perovskite films using the grazing-incidence wide-angle X-ray scattering (GIWAXS) technique. As depicted in Figures 2j−2l for the FAMA, Cs, and PMA samples, respectively, we observed normal 3D signatures of the ringing patterns for the FAMA and Cs samples. In contrast, distinct and sharp Bragg diffraction spots were observed for the PMA sample. In addition, the Bragg diffraction spots such as the (100), (010), (110), and (200) facets align almost parallel to the in-plane momentum transfer vector (q_{xy}). This alignment underscores the well-ordered crystal structure of the 1D perovskite arrays. The PMA cation thus plays an important role to exhibit a preferred orientation along the cubic (100) plane, which is advantageous for enhanced carrier transport inside the perovskite layer.

Figure 3a shows a slight increase in the visible light absorption following the addition of Cs^+ and PMA^+, providing further support for the efficiency enhancement of the PMA device. The absorption spectra show also a minor red-shift with the addition of Cs^+ and PMA^+, corresponding to a slight decrease in E_g. The Tauc plot method was employed to determine the values of E_g, as shown by the results in Figure 3b. The PL spectra reveal that the introduction of Cs^+ and PMA^+ causes a slight red-shift in the emission spectra of the three samples, which agree well with the E_g values determined from the Tauc plot shown in Figure 3b. The optimal perovskite has the PMA composition with a suitable bandgap of 1.93 eV. Through ultraviolet photoelectron spectroscopy (UPS) studies (Figure S10), we determined the energy levels of the valence band maximum (VBM) in this series of perovskites.[14] As shown in Figure S10, the binding energy of valence band electrons shows a slight decrease with the addition of Cs^+ and PMA^+, but this change is insignificant in influencing the VBM levels. There is a noticeable downward shift in the samples' work functions upon adding Cs^+ and PMA^+, suggesting an elevated position of the Fermi energy level, but the scale of energy level elevation is rather small (Figure S10). To determine the conduction band minimum (CBM) values, the E_g values obtained from Tauc plots were added to the VBM values for each perovskite sample. Figure 3c shows the VBM

https://doi.org/10.1021/acsenergylett.4c00796
ACS Energy Lett. 2024, 9, 2351−2357

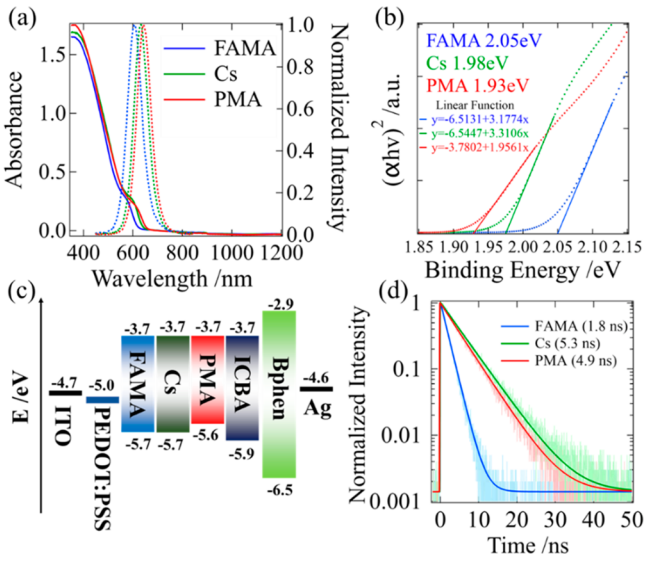

Figure 3. (a) UV−vis absorption and PL; (b) Tauc plots of the FAMA, Cs, and PMA samples; (c) energy level diagram of different perovskites and other charge transport layers in a TPSC;[14] (d) and TCSPC decay profiles of the FAMA, Cs, and PMA films.

and CBM levels for the three perovskites to compare with those of the other charge transport layers and electrodes.

To further investigate the recombination times of photo-excited electron−hole pairs of this series of perovskites, we carried out time-correlated single photon counting (TCSPC) measurements to determine the PL lifetimes for the FAMA, Cs, and PMA samples.[14] The TCSPC results were fitted with a single exponential decay function (Figure 3d) and the fitted time coefficients are listed in Table S2. The PL lifetimes of FAMA, Cs and PMA perovskites were fitted to be 1.8, 5.3, and 4.9 ns, respectively. The increase of PL lifetime between Cs and FAMA can be attributed to improved grain sizes with fewer defect states, whereas a slight decrease of the PL lifetime of PMA compared to that of Cs is because of quasi-2D structure induced by the PMA cation that might lead to an efficient charge separation for the PMA sample. An increased PL lifetime suggests that the electrons remained in the CBM for a longer duration. Therefore, the charge recombination between electrons and holes was retarded to enhance the device performance for the Cs and PMA devices compared to the FAMA device.

Femtosecond transient absorption spectra (TAS) of the FAMA, Cs, and PMA samples with PEDOT:PSS as an underlayer were investigated; a detailed description and discussion of the TAS results are given in Figures S11 and S12. In summary, the optical properties estimated from both TCSPC and TAS together suggest that inferior performance of the FAMA sample is due to rapid carrier recombination, which can be improved by the addition of Cs cations, but the charge transport properties of the latter are shown to be modest, and they can be further improved by the addition of PMA cations as their TAS results show efficient hot-hole injection to the PEDOT:PSS layer (Figure S12).

After optimizing the chemical structures for the quadruple-cation wide-bandgap tin perovskites with cations FA/MA/Cs/PMA and anions Br_2I, we fixed the quadruple-cation cation composition (PMA) but varied the halide cations with Br_3, Br_2I (as a reference), BrI_2, and I_3 and performed their film characterizations and corresponding device optimizations. The detailed descriptions and related discussion on these halide samples are given in Figures S13−S27 and Tables S3−S10. Basically, replacing Br with I decreases the bandgap of the perovskite and vice versa, giving the bandgaps 2.38, 1.93, 1.60, and 1.34 eV for Br_3, Br_2I, BrI_2, and I_3, respectively. All the measurements shown in the Supporting Information indicate that the Br_2I perovskite has the best optoelectronic characteristics suitable for a wide-bandgap TPSC.

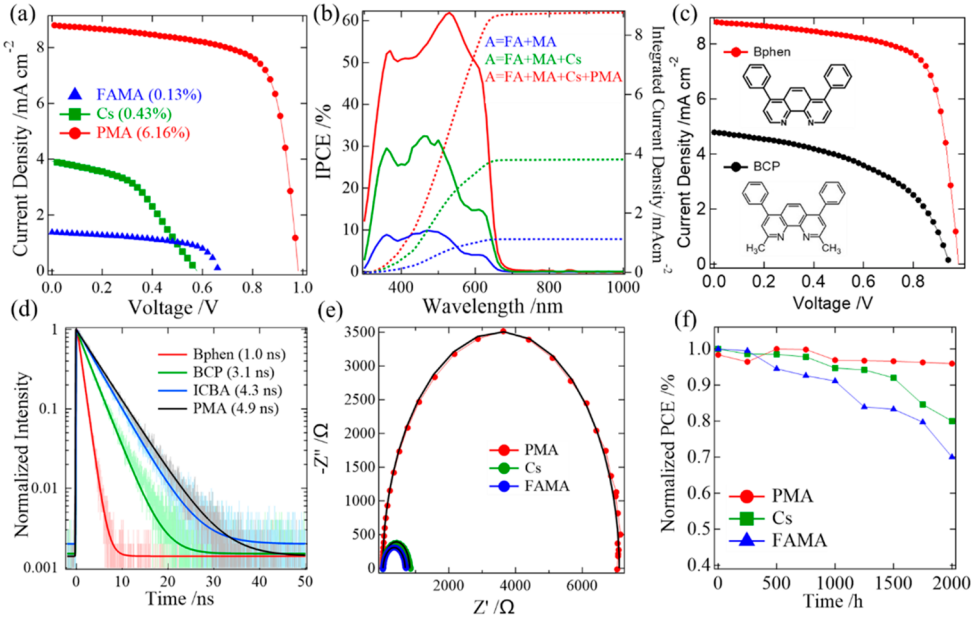

Figure 4. (a) *J*−*V* characteristic curves and (b) IPCE spectra of the FAMA, Cs, and PMA devices; (c) *J*−*V* measurements of TPSC with BCP and Bphen as hole block layer; (d) PL decay profiles of TCSPC of perovskite (PMA) only, PMA with ICBA (ICBA), PMA with ICBA+BCP (BCP), and PMA with ICBA+Bphen (Bphen); (e) Nyquist plots from EIS measurements; and (f) normalized plots of PCE vs shelf-storage period showing the long-term stability of the FAMA, Cs, and PMA devices.

https://doi.org/10.1021/acsenergylett.4c00796
ACS Energy Lett. 2024, 9, 2351−2357

The devices were fabricated according to the structure of ITO/PEDOT:PSS/perovskite/ICBA/Bphen/Ag. Figure 4a shows the $J-V$ characteristics of the devices made of FAMA, Cs, and PMA perovskites. The PCE of the FAMA device shows poorly 0.13%, and with addition of Cs^+, the PCE of the Cs device increases to only 0.43%. However, when both Cs^+ and PMA^+ were added to FAMA, the PCE of the PMA device was enhanced to a remarkable value, 6.2%. Figure 4b shows IPCE spectra, for which their integrated current densities agree well with those obtained from the $J-V$ measurements. ICBA was selected as an electron transport layer because its energy level matches with the CBM levels of those Br_2I perovskites (Figure 3c); thus, it can reduce the voltage loss to improve the V_{OC} of the device.[16−18] Nevertheless, in the Br_2I system, the ICBA−BCP combination faced challenges in efficiently extracting electrons from the perovskite. As shown in Figure 4c, when Bphen was used as a barrier layer for this series of TPSCs, the electron extraction became much more efficient than BCP to enhance the J_{SC} and overall device performance for the former than for the latter. We therefore demonstrate for the first time a wide-bandgap lead-free TPSC (E_g = 1.93 eV) with a quadruple-cation cationic and mixed-halide structure to give a PCE exceeding 6%.

To gain a deeper understanding of electron transfer dynamics between the electron conducting layer (ICBA) and the hole blocking layer (Bphen), TCSPC measurements were performed on the four samples (PMA, PMA+ICBA, PMA +ICBA+BCP, and PMA+ICBA+Bphen), with the PL decay profiles shown in Figure 4d. The data were analyzed using the single exponential decay function, and the fitted time coefficients are listed in Table S3. The PL lifetime of PMA is 4.9 ns, and it decreases to 4.3 ns when PMA was in contact with ICBA, indicating electron extraction by ICBA alone has a poor effect. When both ICBA and BCP were added on PMA, the lifetime decreased to 3.1 ns, indicating a certain effect on hole blocking from perovskite to the Ag electrode. When ICBA and Bphen were added on PMA, the lifetime significantly decreased to 1.0 ns, indicating the great power of hole blocking for the PMA+ICBA+Bphen film to improve the electron extraction from perovskite to the Ag electrode.

Electrochemical impedance spectroscopy (EIS) studies were conducted to analyze the charge recombination characteristics for this series of TPSCs. These EIS measurements were carried out in dark conditions at a bias voltage of 0.5 V. As depicted in Figure 4e, Nyquist plots of all devices featured only a single semicircle, which was modeled using a simple RC equivalent circuit model. The derived impedances show a trend with the order PMA > Cs > FAMA, indicating that the ability to retard the charge recommendation should follow the same order. The EIS results reasonably explain the great performance on V_{OC}, J_{SC}, and PCE of the PMA device compared to those of the other two devices.

The reproducibility of the device performance is shown as boxplots in Figure S28 with 30 devices for each sample (FAMA, Cs, and PMA) under identical experimental conditions; the photovoltaic parameters of these devices are summarized in Tables S11−S13. Figure 4f shows the shelf-storage stability for each device stored in a glovebox for 2000 h. It clearly shows that the PMA device retains over 95% of the initial performance, which outperforms the other two devices with much poorer device performances. The PMA device with a film thickness of the perovskite layer of 190 nm (Figure S30) also displays little effect of hysteresis (Figure S29 and Table S6), making it a suitable candidate as a high-bandgap TPSC for future application in a lead-free all-perovskite tandem solar cell.

In conclusion, we developed a wide-bandgap TPSC system with a quadruple-cation perovskite configuration involving four A-site cations (FA/MA/Cs/PMA) and two X-site anions (Br_2I) to give a bandgap of 1.93 eV. The Br_2I structure is crucial to adjust the bandgap to the desired range of 1.8−2.0 eV. However, light-induced halide segregation resulted in bandgap instability,[22] as the PL spectra of the three samples (FAMA, Cs, and PMA) after light irradiation for 5 min (Figure S31) have shown. The addition of MA and Cs can help to improve phase separation, but their film morphology and crystallinity were not good enough to enhance their device performances. The addition of PMA plays a pivotal role in forming a quasi-2D structure not only on the surface of the perovskite but also in the bottom interface between perovskite and PEDOT:PSS based on the evidence obtained from XPS, SEM, GIWAXS, and TOF-SIMS measurements. Therefore, PMA had the effect to passivate the surface defects, to avert Sn^{2+}/Sn^{4+} oxidation, and to prevent migration of bromine anions for keeping phase stability of the Br-rich system. Moreover, TCSPC and TAS measurements ensure that the PMA film has a longer PL lifetime with fewer defect states and rapid hot-hole injection from perovskite to PEDOT:PSS. As a result, the PMA device with ICBA as an electron-extraction material and Bphen as hole-blocking material attained a PCE of 6.2% with shelf-stability retaining over 95% of initial performance for 2000 h. This is the first wide-bandgap TPSC with a quadruple-cation composition reported to be suitable for future lead-free perovskite tandem solar cell applications.

■ ASSOCIATED CONTENT

Supporting Information

The Supporting Information is available free of charge at https://pubs.acs.org/doi/10.1021/acsenergylett.4c00796.

Description of optimization procedure; experimental details; and results of TOPAS, UPS, TAS, FTIR, SEM, XRD, UV−vis absorption/PL spectra, TCSPC, Raman spectrum, TOF-SIMS, energy level diagrams, $J-V$ curves, IPCE spectra, boxplots of photovoltaic parameters, EIS, and forward and reverse $J-V$ scans (PDF)

■ AUTHOR INFORMATION

Corresponding Author

Eric Wei-Guang Diau − *Department of Applied Chemistry and Institute of Molecular Science and Center for Emergent Functional Matter Science, National Yang Ming Chiao Tung University, Hsinchu 300093, Taiwan;* orcid.org/0000-0001-6113-5679; Email: diau@nycu.edu.tw

Authors

Chun-Hsiao Kuan − *Department of Applied Chemistry and Institute of Molecular Science, National Yang Ming Chiao Tung University, Hsinchu 300093, Taiwan*

Yu-Cheng Chen − *Department of Applied Chemistry and Institute of Molecular Science, National Yang Ming Chiao Tung University, Hsinchu 300093, Taiwan*

Sudhakar Narra − *Department of Applied Chemistry and Institute of Molecular Science, National Yang Ming Chiao Tung University, Hsinchu 300093, Taiwan;* orcid.org/0000-0003-4893-9204

https://doi.org/10.1021/acsenergylett.4c00796
ACS Energy Lett. 2024, 9, 2351−2357

Chun-Fu Chang − *Department of Applied Chemistry and Institute of Molecular Science, National Yang Ming Chiao Tung University, Hsinchu 300093, Taiwan;* orcid.org/0000-0001-7750-220X
Yi-Wei Tsai − *National Synchrotron Radiation Research Center, Hsinchu 30076, Taiwan*
Jhih-Min Lin − *National Synchrotron Radiation Research Center, Hsinchu 30076, Taiwan*
Guan-Ruei Chen − *National Synchrotron Radiation Research Center, Hsinchu 30076, Taiwan*

Complete contact information is available at: https://pubs.acs.org/10.1021/acsenergylett.4c00796

Notes

The authors declare no competing financial interest.

■ ACKNOWLEDGMENTS

We thank Mr. C.-C. Wang (Instrumentation Center, NTHU) for the assistance on TOF-SIMS measurements. We thank Prof. C.-S. Lin and Ms. Y.-T. Lee of the Instrumentation Center, National Taiwan University for FEG-SEM experiments. We also thank Dr. Y.-W. Tsai and Dr. J.-M. Lin (TPS 25A1 NSRRC) for their kind assistance in GIWAXS data analysis. We also thank Dr. C.-H. Wang and Dr. B.-H. Liu (TLS 24A1 NSRRC) for their kind assistance in XPS and UPS measurements. We appreciate Dr. P.-Y. Huang and Dr. Y.-C. Lee (TLS 14A1 NSRRC) for their kind assistance in FTIR analysis. We gratefully acknowledge the support by the National Science and Technology Council (NSTC), Taiwan (Grant NSTC 111-2634-F-A49-007, NSTC 111-2123-M-A49-001, and NSTC 112-2639-M-A49-001-ASP) and the Center for Emergent Functional Matter Science of National Yang-Ming Chiao Tung University (NYCU) from the Featured Areas Research Center Program within the framework of the Higher Education Sprout Project by the Ministry of Education (MOE) in Taiwan.

■ REFERENCES

(1) Best Research-Cell Efficiency Chart | Photovoltaic Research | NREL. https://www.nrel.gov/pv/cell-efficiency.html (accessed 2024-03-14).
(2) Jiang, Q.; Tirawat, R.; Kerner, R. A.; Gaulding, E. A.; Xian, Y.; Wang, X.; Newkirk, J. M.; Yan, Y.; Berry, J. J.; Zhu, K. Towards linking lab and field lifetimes of perovskite solar cells. *Nature* **2023**, *623* (7986), 313−318.
(3) Jiang, Q.; Tong, J.; Scheidt, R. A.; Wang, X.; Louks, A. E.; Xian, Y.; Tirawat, R.; Palmstrom, A. F.; Hautzinger, M. P.; Harvey, S. P.; Johnston, S.; Schelhas, L. T.; Larson, B. W.; Warren, E. L.; Beard, M. C.; Berry, J. J.; Yan, Y.; Zhu, K. Compositional texture engineering for highly stable wide-bandgap perovskite solar cells. *Science* **2022**, *378* (6626), 1295−1300.
(4) Lin, R.; Wang, Y.; Lu, Q.; Tang, B.; Li, J.; Gao, H.; Gao, Y.; Li, H.; Ding, C.; Wen, J.; Wu, P.; Liu, C.; Zhao, S.; Xiao, K.; Liu, Z.; Ma, C.; Deng, Y.; Li, L.; Fan, F.; Tan, H. All-perovskite tandem solar cells with 3D/3D bilayer perovskite heterojunction. *Nature* **2023**, *620* (7976), 994−1000.
(5) Liu, C.; Yang, Y.; Chen, H.; Xu, J.; Liu, A.; Bati, A. S.; Zhu, H.; Grater, L.; Hadke, S. S.; Huang, C.; Sangwan, V. K.; Cai, T.; Shin, D.; Chen, L. X.; Hersam, M. C.; Mirkin, C. A.; Chen, B.; Kanatzidis, M. G.; Sargent, E. H. Bimolecularly passivated interface enables efficient and stable inverted perovskite solar cells. *Science* **2023**, *382* (6672), 810−815.
(6) Li, T.; Xu, J.; Lin, R.; Teale, S.; Li, H.; Liu, Z.; Duan, C.; Zhao, Q.; Xiao, K.; Wu, P.; Chen, B.; Jiang, S.; Xiong, S.; Luo, H.; Wan, S.; Li, L.; Bao, Q.; Tian, Y.; Gao, X.; Xie, J.; Sargent, E. H.; Tan, H. Inorganic wide-bandgap perovskite subcells with dipole bridge for all-perovskite tandems. *Nat. Energy* **2023**, *8* (6), 610−620.
(7) Xu, J.; Boyd, C. C.; Yu, Z. J.; Palmstrom, A. F.; Witter, D. J.; Larson, B. W.; France, R. M.; Werner, J.; Harvey, S. P.; Wolf, E. J.; et al. Triple-halide wide−band gap perovskites with suppressed phase segregation for efficient tandems. *Science* **2020**, *367* (6482), 1097−1104.
(8) Diau, E. W.-G.; Jokar, E.; Rameez, M. Strategies to improve performance and stability for tin-based perovskite solar cells. *ACS Energy Lett.* **2019**, *4* (8), 1930−1937.
(9) Chen, M.; Kapil, G.; Wang, L.; Razey Sahamir, S.; Baranwal, A. K.; Nishimura, K.; Sanehira, Y.; Zhang, Z.; Akmal Kamarudin, M.; Shen, Q.; Hayase, S. High performance wide bandgap Lead-free perovskite solar cells by monolayer engineering. *Chem. Eng. J.* **2022**, *436*, No. 135196.
(10) Teng, T.-Y.; Hu, F.; Lou, Y.-H.; Cao, J.-J.; Chen, C.-H.; Shi, Y.-R.; Wang, K.-L.; Chen, J.; Wang, Z.-K.; Liao, L.-S. Repaired surface structural imperfection of tin Wide-Bandgap perovskite films for photovoltaic application. *Chem. Eng. J.* **2023**, *457*, No. 141292.
(11) Yang, P.; Sun, C.; Fu, X.; Cheng, S.; Chen, J.; Zhang, H.; Nan, Z.-A.; Yang, J.; Zhao, X.-J.; Xie, L.-Q.; Meng, L.; Tian, C.; Wei, Z. Efficient Tin-Based Perovskite Solar Cells Enabled by Precisely Synthesized Single-Isomer Fullerene Bisadducts with Regulated Molecular Packing. *J. Am. Chem. Soc.* **2024**, *146* (4), 2494−2502.
(12) Liu, X.; Wu, T.; Luo, X.; Wang, H.; Furue, M.; Bessho, T.; Zhang, Y.; Nakazaki, J.; Segawa, H.; Han, L. Lead-free perovskite solar cells with over 10% efficiency and size 1 cm2 enabled by solvent−crystallization regulation in a two-step deposition method. *ACS Energy Lett.* **2022**, *7* (1), 425−431.
(13) Kuan, C.-H.; Chih, J.-M.; Chen, Y.-C.; Liu, B.-H.; Wang, C.-H.; Hou, C.-H.; Shyue, J.-J.; Diau, E. W.-G. Additive Engineering with Triple Cations and Bifunctional Sulfamic Acid for Tin Perovskite Solar Cells Attaining a PCE Value of 12.5% without Hysteresis. *ACS Energy Lett.* **2022**, *7* (12), 4436−4442.
(14) Jokar, E.; Chien, C. H.; Tsai, C. M.; Fathi, A.; Diau, E. W. G. Robust tin-based perovskite solar cells with hybrid organic cations to attain efficiency approaching 10%. *Adv. Mater.* **2019**, *31* (2), No. 1804835.
(15) Jokar, E.; Chien, C.-H.; Fathi, A.; Rameez, M.; Chang, Y.-H.; Diau, E. W.-G. Slow surface passivation and crystal relaxation with additives to improve device performance and durability for tin-based perovskite solar cells. *Energy Environ. Sci.* **2018**, *11* (9), 2353−2362.
(16) Jiang, X.; Wang, F.; Wei, Q.; Li, H.; Shang, Y.; Zhou, W.; Wang, C.; Cheng, P.; Chen, Q.; Chen, L.; Ning, Z. Ultra-high open-circuit voltage of tin perovskite solar cells via an electron transporting layer design. *Nat. Commun.* **2020**, *11* (1), 1245.
(17) Jiang, X.; Li, H.; Zhou, Q.; Wei, Q.; Wei, M.; Jiang, L.; Wang, Z.; Peng, Z.; Wang, F.; Zang, Z.; et al. One-step synthesis of SnI_2·(DMSO)x adducts for high-performance tin perovskite solar cells. *J. Am. Chem. Soc.* **2021**, *143* (29), 10970−10976.
(18) Yu, B. B.; Chen, Z.; Zhu, Y.; Wang, Y.; Han, B.; Chen, G.; Zhang, X.; Du, Z.; He, Z. Heterogeneous 2D/3D tin-halides perovskite solar cells with certified conversion efficiency breaking 14%. *Adv. Mater.* **2021**, *33* (36), No. 2102055.
(19) Chen, X.; Jia, Z.; Chen, Z.; Jiang, T.; Bai, L.; Tao, F.; Chen, J.; Chen, X.; Liu, T.; Xu, X.; Yang, C.; Shen, W.; Sha, W. E. I.; Zhu, H.; Yang, Y. M. Efficient and reproducible monolithic perovskite/organic tandem solar cells with low-loss interconnecting layers. *Joule* **2020**, *4* (7), 1594−1606.
(20) Berger, F. J.; Poli, I.; Aktas, E.; Martani, S.; Meggiolaro, D.; Gregori, L.; Albaqami, M. D.; Abate, A.; De Angelis, F.; Petrozza, A. How halide alloying influences the optoelectronic quality in tin-halide perovskite solar absorbers. *ACS Energy Lett.* **2023**, *8* (9), 3876−3882.
(21) Hao, F.; Stoumpos, C. C.; Cao, D. H.; Chang, R. P.; Kanatzidis, M. G. Lead-free solid-state organic−inorganic halide perovskite solar cells. *Nat. photonics* **2014**, *8* (6), 489−494.
(22) Martani, S.; Zhou, Y.; Poli, I.; Aktas, E.; Meggiolaro, D.; Jimenez-Lopez, J.; Wong, E L.; Gregori, L.; Prato, M.; Di Girolamo, D.; Abate, A.; De Angelis, F.; Petrozza, A. Defect Engineering to

Achieve Photostable Wide Bandgap Metal Halide Perovskites. *ACS Energy Lett.* **2023**, *8* (6), 2801−2808.

https://doi.org/10.1021/acsenergylett.4c00796
ACS Energy Lett. 2024, 9, 2351−2357